

# Ultrafast domain dilation induced by optical pumping in ferromagnetic CoFe/Ni multilayers

Dmitriy Zusin<sup>1,\*</sup>, Ezio Iacocca<sup>2,3</sup>, Loïc Le Guyader<sup>4,5</sup>, Alexander H. Reid<sup>4,6</sup>, William F. Schlotter<sup>6</sup>, Tian-Min Liu<sup>4</sup>, Daniel J. Higley<sup>4</sup>, Giacomo Coslovich<sup>6</sup>, Scott F. Wandel<sup>6,\*</sup>, Phoebe M. Tengdin<sup>1</sup>, Sheena K. K. Patel<sup>7,8</sup>, Anatoly Shabalin<sup>7</sup>, Nelson Hua<sup>7,8</sup>, Stjepan B. Hrkac<sup>7</sup>, Hans T. Nembach<sup>9</sup>, Justin M. Shaw<sup>9</sup>, Sergio A. Montoya<sup>8</sup>, Adam Blonsky<sup>1</sup>, Christian Gentry<sup>1</sup>, Mark A. Hofer<sup>3</sup>, Margaret M. Murnane<sup>1</sup>, Henry C. Kapteyn<sup>1</sup>, Eric E. Fullerton<sup>8</sup>, Oleg Shpyrko<sup>7</sup>, Hermann A. Dürr<sup>10</sup>, T. J. Silva<sup>9</sup>

February 13, 2020

<sup>1</sup> Department of Physics and JILA, University of Colorado, Boulder, CO 80309, USA

<sup>2</sup> Department of Mathematics, Physics, and Electrical Engineering, Northumbria University, Newcastle upon Tyne, NE1 8ST, UK

<sup>3</sup> Department of Applied Mathematics, University of Colorado, Boulder, CO 80309, USA

<sup>4</sup> Stanford Institute for Materials and Energy Sciences, SLAC National Accelerator Laboratory, 2575 Sand Hill Road, Menlo Park, CA 94025, USA

<sup>5</sup> Spectroscopy & Coherent Scattering, European X-Ray Free-Electron Laser Facility GmbH Holzkoppel 4, 22869 Schenefeld, Germany

<sup>6</sup> Linac Coherent Light Source, SLAC National Accelerator Laboratory, 2575 Sand Hill Road, Menlo Park, CA 94025, USA

<sup>7</sup> Department of Physics, University of California San Diego, La Jolla, California 92093, USA

<sup>8</sup> Center for Memory and Recording Research, University of California San Diego, La Jolla, California 92093, USA

<sup>9</sup> Quantum Electromagnetics Division, National Institute of Standards and Technology, Boulder, Colorado 80305, USA

<sup>10</sup> Department of Physics and Astronomy, Uppsala University, S-75120 Uppsala, Sweden

---

\* Current address: MIT Lincoln Laboratory, 244 Wood Street, Lexington, MA 02421, USA

**Ultrafast optical pumping of systems with spatially nonuniform magnetic textures is known to cause far-from-equilibrium spin transport effects, such as the broadening of domain-walls. Here, we study the dynamics of labyrinth domain networks in ferromagnetic CoFe/Ni multilayers subject to a femtosecond optical pump and find an ultrafast domain dilation by 6% within 1.6 ps. This surprising result is based on the unambiguous determination of a harmonically-related shift of ultrafast magnetic X-ray diffraction for the first- and third-order rings. Domain dilation is plausible from conservation of momentum arguments, whereby inelastic scattering from a hot, quasi-ballistic, radial current transfers momentum to the magnetic domains. Our results suggest a potentially rich variety of unexpected physical phenomena associated with far-from-equilibrium inelastic electron-magnon scattering processes in the presence of spin textures.**

The understanding of ultrafast magnetisation processes [1, 2, 3, 4, 5, 6, 7, 8, 9, 10] challenges typical notions of non-equilibrium spin dynamics. Many theoretical models and mechanisms have been proposed to explain experimental findings, including heat redistribution in the quasi-equilibrium spin, electronic, and lattice systems [1, 2, 3], superdiffusive spin currents into metallic spin sinks [4, 11], Elliott-Yafet scattering [4], hot-electron transport [5, 6], ultrafast magnon generation and exchange splitting reduction [7], and the femtosecond transition from ferro- to paramagnetic state [9, 10].

The impact of morphological and magnetic spatial inhomogeneities on ultrafast processes has been recognised in studies that rely not only on spatially-averaged measurements, e.g., X-ray magnetic circular dichroism (XMCD) but also on the diffracted X-ray intensity [12, 13, 14, 15]. Transport mechanisms [11, 16, 17] have been proposed to be important in describing spatially-dependent ultrafast phenomena, such as the demagnetisation and domain-wall broadening in domain networks [14, 15, 18], and the imprinting of domain patterns in ferrimagnetic metallic alloys [12, 13]. A time-dependent shift in the scattering ring radius was observed in Ref. [13]. The shift was associated with the transition from a morphologically-induced magnetisation pattern into nonlinear magnetisation structures upon partial quenching of a homogeneously magnetised ferrimagnet. In Ref. [14], an observed ultrafast shift of the first-order X-ray magnetic diffraction ring in the case of a labyrinth domain network was attributed to broadening of fixed domain-walls [18].

Here, we detect time-resolved X-ray diffraction out to the fifth-order ring by use of labyrinth domain networks in a CoFe/Ni multilayer with perpendicular magnetic anisotropy. This allows us to unambiguously detect a 6% shift in the diffraction ring radii within 1.6 ps after pumping. The shift scales harmonically with the diffraction ring order, which is strong evidence for an ultrafast modification of the average domain period. Concurrently, the domain correlation length also shrinks, further evidence for ultrafast spatial alteration of the domain structure.

Domain dilation would require domain-wall speeds deemed unphysical within currently accepted models based on quasi-equilibrium torque transfer [19, 20]. However, domain dilation

is plausible within the framework of inelastic scattering between hot electrons and the spin texture. In the reference frame of outwardly propagating, quasi-ballistic hot electrons subject in a thermal gradient, the domain network appears as a large-amplitude, counter-propagating spin wave with a well-defined momentum. Momentum-conserving scattering between these two systems is sufficient to explain the measured dilation. The detection of such a scattering process in this type of experiment is made possible by the finite size of the pump spot; an important experimental feature that has been heretofore ignored in the analysis of ultrafast pump-probe demagnetisation studies. The proposed scattering mechanism motivates further experimental studies that can take advantage of the reciprocal space structure for more exotic spin textures, such as skyrmion lattices and periodic chiral domain structures.

We measured the picosecond time-evolution of the labyrinth domain network by use of pump-probe coherent, time-dependent, soft-X-ray small-angle scattering at the Linac Coherent Light Source (LCLS) free-electron laser. The sample was a 40 nm thick CoFe/Ni multilayer with perpendicular uniaxial anisotropy. A high-speed CCD camera captures the time-dependent scalar diffracted intensity of the probe beam. The experimental setup is schematically shown in Figure 1a.

The time-evolution of the labyrinth domain network is inferred from the magnetic scattering squared amplitude  $|S(\mathbf{q}, t)|^2$ , with wavevector  $\mathbf{q}$ , isolated from the diffracted intensity  $I(\mathbf{q}, t)$  by subtracting the charge intensity  $|C(\mathbf{q}, t)|^2$  obtained from the saturated sample, as described in the Supplementary Note 1. Details on the samples' preparation, setup, and measurement technique are given in the Methods. For labyrinth domains randomly oriented in the film's plane,  $|S(\mathbf{q}, t)|^2$  consists of concentric rings, shown in Figure 1b. The width of each diffraction ring results from the domain-size distribution, akin to jitter in temporal signals [21]. We note that the first-order scattering ring was partially obscured by the location of the through-beam aperture in the centre of the CCD camera, depicted as a dark-blue box in Figure 1b.

We azimuthally average the magnetic scattering intensity to obtain  $S^2(q, t)$ , where  $q = |\mathbf{q}|$  (See details in Methods). The pre-pump ( $t < 0$ ) average data is shown in Figure 1c by a solid black line. The shoulder in the first-order diffraction ring at  $q < 0.0375 \text{ nm}^{-1}$ , shown by a grey area, is an artefact of the aforementioned partial obscuration by the aperture.

The shape of  $S^2(q, t)$  is fitted by the function  $f(q, t)$ , composed of two factors:

$$f(q, t) = e^{-2q/Q(t)} \left[ M_0(t) + \sum_{n=0}^2 \frac{M_{2n+1}(t)}{\left( \frac{q - (2n+1)q_0(t)}{(2n+1)\Gamma(t)} \right)^2 + 1} \right]^2 \quad (1)$$

The first is the exponential form factor associated with the non-zero characteristic spin correlation length scale,  $Q(t)$ . The second term is the magnetic structure factor, consisting of a linear superposition of inhomogeneities with uniform spectrum originating from the sample's morphology,  $M_0(t)$ , and three Lorentzians centred at odd-integer multiples of the first-order ring,  $q_0(t)$ , as enforced by Fourier series decomposition. The quantities  $M_{2n+1}(t)$  are fitting parameters that are proportional to the harmonic rings' amplitudes with indices denoting the

respective diffraction order.  $\Gamma(t)$  is the linewidth associated with the domain-size correlation length. We stress that the function  $f(q,t)$  is an empirical fit to the magnetic scattering intensity.

The concurrent fit of the three diffraction rings and the form factor is essential to accurately determine the fitting parameters. The fit of the time-averaged  $t < 0$  diffraction data by use of equation (1) is shown in Figure 1c with the red dashed curve. The exponential form factor contribution of  $Q(0) = 0.1087 \text{ nm}^{-1} \pm 4 \times 10^{-5} \text{ nm}^{-1}$  is shown by a dashed blue line. The fitted first-order ring radius is  $q_0(0) = 0.0392 \text{ nm}^{-1} \pm 2 \times 10^{-5} \text{ nm}^{-1}$ , equivalent to an equilibrium domain width of  $\pi/q_0 = 80.1 \text{ nm} \pm 0.01 \text{ nm}$ . Magnetic force microscopy imaging of the labyrinth domain network agrees well with this average domain width, see Supplementary Note 2. To illustrate the quality of the fitting, we show the scattering signal in Figure 1d using an equalized representation

$$S_e(q, t) = \left( \sqrt{S^2(q, t)} e^{q/Q} - M_0(t) \right) q^{2.12} \quad (2)$$

where the exponential form factor is divided out, the magnetic noise background  $M_0(t)$  is subtracted, and the scale factor  $q^{2.12}$  equalizes the amplitudes of the first-order and third-order rings. By use of this equalization, it is visibly apparent that all diffraction rings are fitted with high fidelity. The individual Lorentzian components are shown with solid blue curves.

We apply equation (1) to fit the *time-dependent*, azimuthally averaged scattering signal. In Figure 2a to c, we show the fitting results in the form of  $S_e(q, t)$  at selected times. In all panels, the diffraction amplitudes are quenched, c.f. Figure 1d, as expected for ultrafast demagnetisation. The time-evolution of the form factor is shown in Supplementary Note 3. The full temporal evolution of the normalized amplitudes  $M_{1,3,5}(t)/M_{1,3,5}(t=0)$  is shown in Figure 2d, exhibiting distinct time evolutions. At 1.6 ps, the third-order ring is quenched slightly more than the first-order ring while the fifth-order ring appears to be almost entirely quenched. Both the first-order and third-order rings partially recover until 13 ps after quenching. For  $t > 13$  ps, the third-order ring resumes quenching, but at a much slower rate of  $\approx 2\%$  per ps. While the precision of the fifth-order ring is reduced due to the low photon flux at high  $q$ , it is significantly more quenched compared to the first-order and third-order rings at all times, further confirmed by averaging the scattering data over a time-span from 6 ps to 11 ps, shown in the Supplementary Figure 7.

The empirical fit of finite amplitudes for all three diffraction rings allows us to extract quantitative information on the average width of the domain-walls as well as the average domain width. For the domain-wall average width, we consider a one-dimensional, hyperbolic tangent Bloch-wall model applicable for materials with strong perpendicular magnetic anisotropy [22]. To be compatible with our two-dimensional measurements, we use the azimuthally integrated scattering data such that every diffracted photon is considered to lie along the same  $q$  axis, as would be expected for parallel stripe patterns [23]. We then fit the diffraction peak amplitudes with the Bloch-wall model for a 1-d periodic chain of domain-walls of width  $w_w(t)$ ,

$$A_{2n+1}(t) = \frac{\pi m(t) w_w(t)}{2w_d(t)} \text{csch} \left( \frac{\pi(2n+1)w_w(t)}{2w_d(t)} \right) \quad (3)$$

where  $m(t)$  is the magnetisation of infinitely wide domains separated by a Bloch-wall, and  $w_d(t)$  is the width of the domains (see details in Methods). The harmonic-dependent amplitude data is in good agreement to equation (3), with results at selected times shown in Figure 3a in logarithmic scale. We note that the fifth-order ring amplitude has little weight on the overall fit. The evolution of  $m(t)$  is shown in Figure 3b, exhibiting a typical demagnetisation behaviour, but with a faster remagnetisation process than would otherwise be surmised by inspection of the diffraction amplitude data in Figure 2d. The evolution of  $w_w(t)$  is shown in Figure 3c. The initial domain-wall width is 39 nm, in good agreement with a calculated value of 45 nm from Bloch-wall theory, see Methods. We find a significant broadening of the domain-walls from 39 nm to 51 nm (31%) within 1.6 ps, followed by partial recovery towards its original equilibrium value in the first 10 ps after pumping. From 10 ps to 20 ps, the domain-walls resume broadening to approximately 38% of the original equilibrium value, likely because of a reduction in the effective magnetic anisotropy of the sample due to delayed thermal diffusion through the sample thickness (See Supplementary Note 4).

We now turn to the time evolution of the diffraction ring radii. In Figure 4a, we show colour contour plots of the azimuthally averaged magnetic diffraction ring intensity profiles for the first- and third-order rings as a function of both time and  $q$ , divided by the equilibrium form factor. The visible shift in both radii are marked with horizontal lines that indicate the  $q$ -value for the time-averaged ring radii before (dashed red line) and between 6 and 11 ps after optical pumping (dashed black line). The difference in the average radii,  $\delta q$ , is  $0.0018 \pm 0.0001 \text{ nm}^{-1}$  for the first-order ring, and  $0.0054 \pm 0.0003 \text{ nm}^{-1}$  for the third-order ring.

The data and fits depicted in the  $S_e(q, t)$  representation at 0 ps, 1.6 ps, and 18.8 ps are shown in Figure 4b, vertically shifted for clarity. The experimental data are shown with black curves and the fits with dashed red curves. The radii of the diffraction rings at equilibrium are indicated with vertical dashed lines. In this representation, the third-order diffraction ring shift is evident, the position of which is shown by black circles, c.f. vertical dashed black lines. Computing the domain size as  $w_d(t) = \pi/q_0(t)$ , we obtain the time evolution shown in Figure 4c, which exhibits a 6% dilation at 1.6 ps, i.e. an average domain width of 86 nm. We restate that our fitting procedure enforces harmonically related rings, *so that their accurate fits are strong evidence that there is indeed domain dilation at picosecond timescales.*

A reminiscent 4% shift in the first-order diffraction ring radius was previously observed by time-resolved X-ray scattering in a similar magnetic system that supports labyrinth domain patterns [14]. In that work, a domain dilation stemming from the ring radius shift was deemed unphysical due to the exceedingly large domain-wall speeds at the edges of the X-ray probe spot implied by a fractional expansion in the average domain width,  $(0.04 \times 10 \mu\text{m})/1 \text{ ps} = 4 \times 10^5 \text{ m s}^{-1}$ . Such an extreme speed is many orders of magnitude larger than known mechanisms to drive *isolated domain-walls* in equilibrium, e.g. Refs. [19, 20]. Pfau, et al., [14] attributed the diffraction ring radius shift to domain wall broadening, modelled with an effective Gaussian filter function to represent how smaller domains demagnetise more than larger domains. Such a filter function is inconsistent with our data because application of a sufficiently-narrow filter induces a sizeable asymmetry in the diffracted rings profile. An extensive discussion on the harmonic dependent-asymmetry and filter function

implementation is provided in the Supplementary Note 5. Based on the fit to the pre-pump data  $\langle S^2(q, t < 0) \rangle$ , fitting of the time-dependent data with such a Gaussian filter function resulted in the dashed blue curves in Figure 4b, with inferior results.

The persistent ring symmetry after pumping allows for accurate fitting of the correlation length  $\propto 1/\text{linewidth}$ , shown in Figure 4d, from  $2\pi/7.4 \mu\text{m}^{-1} \approx 848 \text{ nm}$  in equilibrium to  $2\pi/8.8 \mu\text{m}^{-1} \approx 722 \text{ nm}$  at 1.6 ps after optical pumping. This is supporting evidence for an ultrafast change in the spatial structure of the domain pattern: the domains must necessarily incur in ultrafast spatial rearrangement for the correlation length to change. We also note that the diffraction rings scattered by stripe domain patterns *in equilibrium* may shift as a consequence of an increased correlation, giving the impression of a net dilation [24]. This possibility can be excluded because the correlation length actually decreases.

While the requisite domain wall speeds to accommodate domain dilation are far beyond what have been previously demonstrated, such speeds do not violate any fundamental physics if one considers momentum and energy exchange between the electronic and spin system. We can examine the plausibility of such exchange by resorting to reciprocal space, where the periodic variation of the magnetic pattern can result in a transfer of linear momentum between electrons and correlated spin textures. For example, one could imagine a mechanism based loosely on inelastic electron-magnon scattering that couples the electronic and spin system in momentum space. We are motivated by the fact that, in the reference frame of a hot quasi-ballistic electron moving in the +x direction, the domain structure of the system incurs a Doppler shift, schematically shown in Figure 5a. In other words, the spin texture is indistinguishable from a non-zero frequency magnon ensemble of that is moving in the -x direction with an average momentum proportional to the first-order ring radius.

Given that the pump pulse creates a substantial *lateral* temperature gradient in the hot electron bath at time  $t = 0$ , the average, instantaneous, non-equilibrium electron momentum in the ballistic limit is  $\langle \mathbf{p}_e(t) \rangle \cong k_B \nabla T t \hat{\mathbf{r}}$  [25], where  $\hat{\mathbf{r}}$  is the radially directed unit vector (See Supplementary Note 6). This approximation is valid for  $t < \tau_{el}$ , where  $\tau_{el}$  is the electron-lattice scattering time in a non-equilibrium scenario. In the rest frame of the electrons, defined by the ensemble average velocity, the initial domain network is a coherent superposition of magnons with non-zero frequency, along with a commensurate momentum per magnon of  $p_m(t = 0) = h/2w_d$ . Invoking conservation of momentum, relaxation of the electronic system back to equilibrium via electron-magnon scattering results in *a coherent recoil of the magnetic system*, i.e. a change of the equivalent magnon momentum given by

$$\Delta p_m(\tau) = p_m - \Delta p_e(\tau) \quad (4)$$

The average electron momentum in equation (4) remains smaller than the magnon momentum, i.e.  $p_m \gg \Delta p_e(\tau)$  such that the resultant magnon recoil results in a perturbation of the equilibrium domain wavelength. If such magnon-electron scattering were present, the process would be analogous to Compton scattering, albeit not relativistic, whereby a magnon can scatter from free electrons resulting in both an energy and momentum shift. Under the assumption of an electronic relaxation process where every available hot conduction electron with excess momentum  $\langle p_e(t) \rangle$  scatters from every available magnon with momentum  $h/2w_d$  (see Methods), we obtain a relative domain dilation of  $2w_d k_B \nabla T \tau / h = 6 \%$  at  $\tau = 1 \text{ ps}$ . For

this calculation, we estimate a *lateral* electronic temperature gradient as approximately 3000 K (See Supplementary Note 4) over the pump spot radius of 172  $\mu\text{m}$ . Therefore, we conclude that there is sufficient momentum in the electronic system such that an inelastic electron-magnon scattering process could cause such a shift in the domain period. It is also the case that the kinetic energy of the hot electron system is sufficient to drive the measured domain dilation, as is also required for inelastic scattering (See Supplementary Note 7).

Two important caveats must be mentioned. First, there is a significant temperature gradient through the sample thickness during the first 2 ps after optical pumping (see Supplementary Figure 4). This implies that domain dilation must be a non-local effect, insofar as the domains are dilated throughout the sample thickness. Otherwise, a disparate domain dilation at the top and bottom surfaces of the sample would disintegrate the domain network, an event that would be experimentally detected as a collapse of the harmonic rings. Second, the electronic thermal gradient within the X-ray *probe* spot is likely much smaller than that expected further from the centre of the pump spot, implying that any electron-magnon scattering must either be non-local in nature, or the quasi-ballistic electron momentum, due to a combination of charge conservation and electrostatic screening, e.g. plasmon dynamics, is not strictly a function of the local temperature gradient.

From the experimental data and the 1-d Bloch wall model in equation (3), we can reconstruct the one-dimensional domain profile dynamics. The domain profile at  $t = 0$  is shown in Figure 5b by a dashed black curve and compared to the profiles at 1.6, 11.2, and 20 ps in solid blue curves, showcasing the magnetisation quench, domain-wall broadening, and domain dilation. The full evolution is available in the Supplementary Movie 1. The time-evolution of the maximum magnetisation within each domain is plotted in Figure 5c by blue circles. The maximum quenching of 50% occurs 1.2 ps after pumping. In contrast, a quenching of only 35% is determined from XMCD measurements under identical pumping conditions, but with the sample subject to an *in situ* saturating magnetic field, shown by red circles in Figure 5c. This difference is further evidence that inelastic electron-magnon scattering is enhanced in the multidomain state. The convergence of both curves after 10 ps is indicative that the dynamics are strictly thermally thereafter.

Considering a static domain network to be equivalent to a magnon distribution, although unconventional, is consistent with the well-defined spectral character of our magnetic sample. The primary assertion that we bring forward is that a static domain network subject to a Doppler shift in the reference frame of moving electrons is no different than a spin-wave with a well-defined momentum. Insofar as the spin texture possesses such a well-defined momentum, i.e., some degree of spatial coherence, inelastic scattering would allow for domain dilation that manifests as extremely large domain-wall speeds in real space. In other words, any such mechanism requires localization in momentum space and, as such, does not apply to isolated domain-walls. The possibility that quasi-ballistic momentum imparted to the electronic system by ultrafast optical pumping suggests that domain dilation should be tuneable by laser fluence and spot size, as well as details of the domain structure, including domain size, domain wall size, and domain orientation. As such, these results greatly expand the parameter space in which to further explore the rich nature of far-from-equilibrium electron-spin interactions,

including materials with more exotic spin textures, such as chiral domain networks and skyrmion lattices.

## Methods

### Experimental setup

The magnetic samples were fabricated by sputter deposition with the following layer composition:  $\text{Si}_3\text{N}_4(50)$  /  $\text{Ta}(3)$  /  $\text{Cu}(5)$  /  $[\text{Co}_{90}\text{Fe}_{10}(0.2)/\text{Ni}(0.6)]\times 50$  /  $\text{CoFe}(0.2)$  /  $\text{Cu}(3)$  /  $\text{Ta}(3)$ , where the layer thicknesses in parentheses are in nm. The  $\text{Si}_3\text{N}_4$  membrane allows for X-ray transmission. X-ray measurements were performed at the SXR hutch [26] at the Linac Coherent Light Source (LCLS). The free-electron laser (FEL) generated 60 fs long soft X-ray pulses at a repetition rate of 120 Hz with a photon energy of 852.7 eV to match the  $L_3$  absorption edge of Ni. Circularly polarized X-rays were achieved by use of a Delta-undulator [27]. The X-ray beam was focused to an elliptical spot with foci  $a = 23 \mu\text{m}$  and  $b = 15 \mu\text{m}$ . The scattered X-rays were recorded with a primary CCD detector placed 275.3 mm away from the sample. The detector had four  $512 \times 512$  pixel panels that could be moved independently from one another. Such an experimental geometry allowed us to detect X-rays scattered at angles of up to  $\approx 8^\circ$ . The camera pixels have a maximum well depth of 16,000 electrons.

The CCD camera had an opening at the centre through which unscattered X-rays were transmitted. These X-rays were detected with a secondary CCD placed behind the primary CCD. An Al filter in front of the secondary CCD was used to suppress the infrared pump beam, which was collinear with the incident X-ray beam. In addition to scattering measurements without an applied magnetic field, we carried out measurements of both the scattering (with the primary CCD) and XMCD (with the secondary CCD) when the sample was magnetically saturated to remove any non-magnetic contributions from the zero-field scattering data [28]. For this, an external magnetic field of 0.6 T was applied perpendicularly to the surface of the sample.

An amplified infrared (IR) laser pump pulse from a Ti:Sapphire laser at the central wavelength of 795 nm was used to pump the sample. The duration of the IR pump pulses was 60 fs, the Gaussian beam waist size was  $172 \mu\text{m}$ , and the average incident pump fluence was  $23 \text{ mJ cm}^{-2}$ . Higher pump fluence resulted in catastrophic damage to the sample. The pump laser was synchronized with the FEL to within the jitter of the arrival time of X-ray pulses. The delay time between the IR pump and the X-ray probe was varied from negative delays (to probe an unperturbed sample before the IR pump has arrived) to 20 ps. Scattering patterns at different delays were collected in a single-shot manner, and the pattern at a given delay was computed as an average of all of the scattering patterns taken within  $\pm 200$  fs of that delay. The first-order diffraction ring contained 500 electrons per shot,  $\approx 3\%$  of the camera saturation.

The magnetic parameters of the 40 nm thick CoFe/Ni ferromagnetic multilayers were measured as a function of temperature with a vibrating sample magnetometer (VSM). At room temperature, we determine a saturation magnetisation  $M_s = 771 \text{ kA m}^{-1}$ , a first-order anisotropy constant  $K_1 = 739 \text{ kJ m}^{-3}$ , and a negative second-order anisotropy constant  $K_2 = -266 \text{ kJ m}^{-3}$ . A non-negligible second-order anisotropy was previously reported for this material system [29]. The net uniaxial anisotropy, including the magnetostatic contribution, is  $99 \text{ kJ m}^{-3}$ .



This corresponds to an effective magnetisation  $M_{\text{eff}} = -2.05 \text{ kA m}^{-1}$  for perpendicular FMR. The experimentally measured FMR value is  $M_{\text{eff}} = -2.12 \text{ kA m}^{-1}$ , in good agreement with the VSM measured value. Despite the large second-order anisotropy constant, the relative magnitudes of the first- and second-order anisotropies are within the range necessary for a net perpendicular magnetic anisotropy [30]. We confirmed that out-of-plane labyrinth domain network is indeed stabilised at room temperature by use of magnetic force microscopy measurements, shown in the Supplementary Figure 1.

### Azimuthal averaging

The azimuthal average of incomplete data captured by the primary CCD camera is performed according to the following algorithm. First, the centre of the scattering pattern,  $|\mathbf{q}| = 0$ , is determined by fitting a circle to the 3<sup>rd</sup> order diffraction ring. Because this diffraction ring was not obscured by the central square aperture, a reliable fit can be obtained for the centre location in pixels. Once the centre is determined, the data is then azimuthally averaged. By definition, the azimuthal average  $\langle S^2(\mathbf{q}, t) \rangle = \left( \int_0^{2\pi} S^2(q \cos \theta, t) d\theta \right) / L(q)$ , where  $\theta$  is the polar angle for the  $\mathbf{q}$  vector and  $L(q)$  is the circumference for a given  $q$ . To account for the missing pixels, we compute  $L(q) = \int_0^{2\pi} W(q, \theta) d\theta$ , where  $W(q, \theta)$  is a two-dimensional mask of the CCD cameras, where missing pixels are numerically counted for as zeros. In this way, the azimuthal average is normalized by an adjusted circumference that does not count missing pixels.

### Bloch wall model

The profile of a single Bloch-type domain-wall is modelled as [22]

$$m_d(x, t) = m(t) \tanh\left(\frac{x}{a(t)}\right) \quad (5)$$

where  $m(t)$  is the time-dependent, normalised magnetisation within the adjacent domains, and  $a(t)$  is a measure of the domain-wall width. Equation (5) is strictly applicable to materials with negligible second-order anisotropy constant. In our case, the ratio between the second and first-order anisotropy constants is  $\kappa = -0.36$ . This ratio leads to a broader domain-wall, yet similar in shape to that predicted from equation (5). See, e.g., Figure 3.60 in Ref. [22]. The domain-wall width is calculated following the Lilley interpretation that considers the slope of the domain-wall profile at the origin [22]. From our fitting parameters, the domain-wall width is defined as  $w_w = \pi a(t)$ . Assuming an exchange constant of  $A_{ex} = 2 \times 10^{11} \text{ J m}^{-1}$ , the calculated domain-wall width from Bloch theory is approximately  $w_w = \pi \sqrt{A_{ex} / (K_1 + K_2)} = 45 \text{ nm}$ , where we consider the reduced anisotropy  $K_1 + K_2$ .

In  $q$ -space, a Bloch wall profile for an individual domain wall in a periodic array of domains of width  $w_d = \pi/q_0$  results in a discrete spectral amplitude given by

$$A_{2n+1}(t) = \frac{\pi^2 m(t) a(t)}{2w_d(t)} \text{csch}\left(\frac{\pi^2 (2n+1) a(t)}{2w_d(t)}\right) \quad (6)$$

We obtain equation (6) by convolving the spectrum of a square wave of periodicity  $w_d = \pi/q_0$  with the spectrum of the derivative of the Bloch-wall model equation (5). Using the domain-wall-width definition of  $w_w = \pi a(t)$ , we obtain equation (3). In this case,  $m(t)$  is the asymptotic magnetisation amplitude in the infinite wavelength limit, i.e. when  $q_0 \rightarrow 0$ . It is not to be confused with the maximum amplitude of the magnetisation between the domains for non-zero  $q_0$ .

To compare our data with this 1-d model, we must consider how the labyrinth domain network distributes the diffracted photons uniformly along the azimuthal coordinate. To account for this, we use azimuthal integration of the measured intensity, where the modelled amplitudes are related to the fitted diffraction ring amplitudes via

$$A_{2n+1}(q_0, t) = M_{2n+1}(t) \sqrt{2\pi(2n+1)q_0} \quad (7)$$

#### Conduction electron density in Co/Ni multilayer

To determine the conduction electron density for our CoFe/Ni multilayers we consider the conduction electron density per layer and perform a volume average. These are obtained from the Hall coefficients for Ni and Co, which are  $-0.61 \times 10^{-10} \text{ m}^3 \text{ C}^{-1}$  and  $-1.33 \times 10^{-10} \text{ m}^3 \text{ C}^{-1}$ , respectively [31]. We assume the Hall coefficient for Co only as the alloy composition is 90% Co and only 10% Fe. From these coefficients, we obtain 1.12 and 0.52 electrons per atom for Ni and Co, respectively. Weighted average of the 3:1 Ni to Co ratio results in 0.97 electrons per atom. Coincidentally, this is approximately equal to the spin density, as well.

#### Data availability

The data that supports the findings of this study are available from the corresponding author upon reasonable request

#### Code availability

Fitting functions were performed both by MATLAB and Mathcad. The codes are available upon reasonable request from E.I. and T.J.S.

## References

- [1] Beaurepaire, E., Merle, J.-C., Daunois, A. & Bigot, J.-Y. Ultrafast spin dynamics in ferromagnetic nickel. *Phys. Rev. Lett.* **76**, 4250 (1996)
- [2] Koopmans, B. et al. Explaining the paradoxical diversity of ultrafast laser-induced demagnetisation. *Nat. Mater.* **9**, 259 – 265 (2009)
- [3] Ostler, T. A. et al. Ultrafast heating as sufficient stimulus for magnetisation reversal in a ferrimagnet. *Nat. Commun.* **3**, 666 (2012)
- [4] Turgut, E. et al. Controlling the competition between optically induced ultrafast spin-flip scattering and spin transport in magnetic multilayers, *Phys. Rev. Lett.* **110**, 197201 (2013)
- [5] Xu, Y. et al. Ultrafast magnetization manipulation using single femtosecond light and hot-electron pulses. *Adv. Mater.* **29**, 1703474 (2107)
- [6] Iihama, S. et al. Single-shot multi-level all-optical magnetization switching mediated by spin transport. *Adv. Mater.* **90**, 220408 (2016)
- [7] Turgut, E. et al. Stoner versus Heisenberg: ultrafast exchange reduction and magnon generation during laser-induced demagnetization. *Phys. Rev. B* **94**, 220408 (2016)
- [8] Zusin, D., et al. Direct measurement of the static and transient magneto-optical permittivity of cobalt across the entire M-edge in reflection geometry by use of polarization scanning. *Phys. Rev. B* **97**, 024433 (2018)
- [9] Eich, S. et al. Band structure evolution during the ultrafast ferromagnet-paramagnetic phase transition in cobalt. *Science Advances* **3**, e1602094 (2017)
- [10] Tengdin, P. et al. Critical behavior within 20 fs drives the out-of-equilibrium laser-induced magnetic phase transition in nickel. *Science Advances* **4**, eaap9744 (2018)
- [11] Battiato, M., Carva, K., and Oppeneer, P.M. Superdiffusive spin transport as a mechanism of ultrafast demagnetisation. *Phys. Rev. Lett.* **105**, 027203 (2010)
- [12] Graves, C. E. et al. Nanoscale spin reversal by nonlocal angular momentum transfer following ultrafast laser excitation in ferrimagnetic GdFeCo. *Nat. Mater.* **12**, 293 – 298 (2013)
- [13] Iacocca, E. et al. Spin-current-mediated rapid magnon localisation and coalescence after ultrafast pumping of ferrimagnetic alloys. *Nat. Commun.* **10**, 1756 (2019)
- [14] Pfau, B. et al. Ultrafast optical demagnetisation manipulates nanoscale spin structure in domain-walls. *Nat. Commun.* **3**, 110 (2012)
- [15] Vodungbo, B. et al. Laser-induced ultrafast demagnetisation in the presence of a nanoscale magnetic domain network. *Nat. Commun.* **3**, 999 (2012)
- [16] Rudolf, D. et al. Ultrafast magnetization enhancement in metallic multilayers driven by superdiffusive spin current. *Nat. Commun.* **3**, 1037 (2012)
- [17] Eschenlohr, A. et al. Ultrafast spin transport as key to femtosecond demagnetization. *Nat. Mater.* **12**, 332 – 336 (2013)

- [18] von Korff Schmising, C. et al. Imaging ultrafast demagnetization dynamics after a spatially localized optical excitation. *Phys. Rev. Lett.* **112**, 217203 (2014)
- [19] Wang, X. S. et al. Domain wall propagation through spin wave emission, *Phys. Rev. Lett.* **109**, 167209 (2012)
- [20] Thiaville, A., Nakatani, Y., Miltat, J. and Suzuki, Y. Micromagnetic understanding of current-driven domain wall motion in patterned nanowires. *Europhys. Lett.* **69**, 990 – 996 (2005)
- [21] Carlson, A., Crilly, P. B. & Rutledge, J. C. *Communication systems: an introduction to signals and noise in electrical communication, Ch. 2, Ch. 11* (McGraw-Hill, New York, 2002)
- [22] Hubert, A. & Schäfer, R. *Magnetic domains: the analysis of magnetic microstructures Ch. 3.* (Springer Verlag, Heidelberg, 2009)
- [23] Hellwig, O., Denbeaux, G. P., Kortright, J. B. and Fullerton, E. E. X-ray studies of aligned magnetic stripe domains in perpendicular multilayers. *Physica B* **336**, 136 – 144 (2003)
- [24] Pierce, M. S. et al. Influence of structural disorder on magnetic domain formation in perpendicular anisotropy thin films. *Phys. Rev. B* **87**, 184428 (2013)
- [25] Najafi, E., et al. Super-diffusion of excited carriers in semiconductors. *Nature Communications* **8**, 15177 (2017)
- [26] Schlotter, W. F. et al. The soft X-ray instrument for materials studied at the linac coherent light source X-ray free-electron laser. *Rev. Sci. Instrum.* **83**, 043107 (2012)
- [27] Lutman, A. A. et al. Polarization control in an X-ray free-electron laser. *Nature Photonics* **10**, 468 – 472 (2016)
- [28] Higley, D. J. et al. Femtosecond X-ray magnetic circular dichroism absorption spectroscopy at an X-ray free electron laser. *Rev. Sci. Instrum.* **87**, 033110 (2016)
- [29] Shaw, J. M., et al. Measurement of orbital asymmetry and strain in Co<sub>90</sub>Fe<sub>10</sub>/Ni multilayers and alloys: Origins of perpendicular anisotropy. *Phys. Rev. B* **87**, 054416 (2013)
- [30] Jang, P.-H., et al. Domain wall dynamics in easy-cone magnets. *Physical Review B* **99**, 024424 (2019)
- [31] Gray, D. E. *AIP Handbook*, 3<sup>rd</sup> edition (AIP, New York, 1972)

## **End notes**

### **Acknowledgements**

This material is based upon work partially supported by the U.S. Department of Energy, Office of Science, Office of Basic Energy Sciences under the X-Ray Scattering Program Awards No. DE-SC0002002 and DE-SC0018237 and Award Number DE-SC0017643. Operation of LCLS is supported by the U.S. Department of Energy, Office of Basic Energy Sciences under contract No. DE-AC02-76SF00515. M.A.H. was partially supported by NSF CAREER DMS-1255422. The authors thank S. Zohar for his support with the data collection and analysis.

### **Author contributions**

M.A.H., M.M.M., H.C.K., E.E.F., O.S., H.A.D., and T.J.S conceived the experiments. D.Z., L.L.G., A.H.R., W.F.S., T.-M.L., D.J.H., G.C., S.F.W., P.M.T., S.K.K.P., A.S., N.H., S.B.H., H.T.N., and T.J.S. performed experiments. J.M.S. and S.A.M. fabricated the samples. A.B., C.G., H.T.N., and T.J.S. characterised the samples. D.Z., E.I., L.L.G., and T.J.S. numerically processed the data. E.I., D.Z., H.A.D., and T.J.S. analysed and interpreted the data. All authors contributed to discussions, data analysis, and writing the manuscript.

### **Competing financial interests**

The authors declare no competing financial interests.

**Figure 1. Experimental setup and static scattering.** **a** A femtosecond infrared (IR) pulse incident on the sample excites the sample. The time-dependent magnetisation is measured by a time-delayed, circularly-polarised X-ray probe. The scattered X-rays are captured by a primary, high-speed CCD while the unscattered beam is captured by a secondary CCD acting as a point detector. An electromagnet is used to saturate the sample, allowing for both measurements of time-resolved XMCD, as well as the static charge contribution to the scattered intensity. **b** The two-dimensional magnetic component of the scattered intensity obtained with the primary CCD. The first-order diffraction ring is partially obscured due to the aperture in the middle of the primary CCD. **c** Equilibrium azimuthally-averaged magnetic scattering. The data, the fit to the data with equation (1), and the fitted form factor are shown by the solid black, dashed red, and dashed blue curves, respectively. The same data and fit are shown in **d** after equalisation, as per equation (2), to accentuate the quality of the fit for all the diffraction rings. The solid blue curves represent the three Lorentzian components of the fit used to determine the periodic structure of the domains. The asymmetry of the Lorentzians is due to equalisation.

**Figure 2. Time evolution of diffraction rings.** The equalised data, fits, and Lorentzians, as per equation (2), are shown by solid black, dashed red, and solid blue curves, respectively. We show three instances in time after pumping: **a** 1.6 ps, **b** 11.2 ps, and **c** 18.8 ps. The horizontal black lines illustrate the relative amplitude of the first- and third-order diffraction rings. **d** Temporal amplitude evolution of the first- (blue), third- (red), and fifth-order (grey) diffraction rings. The vertical dashed lines correspond to the time instances shown in panels **a**, **b**, and **c**. Error bars represent one standard deviation.

**Figure 3. Bloch wall model fits.** **a** Diffraction amplitudes at selected time instances fitted with the Bloch wall model of equation (3). The amplitudes (circles) and fits (crosses) are shown in logarithmic scale and vertically shifted for clarity. From the fits, the evolution of the asymptotic magnetisation,  $m$ , and the domain-wall width,  $w_w$ , are shown in panels **b** and **c**. The colour-coded vertical lines represent the time instances shown in panel **a**. Error bars represent standard deviation. The domain walls broaden by 30% within the first 2 ps after pumping.

**Figure 4. Diffraction ring shifts.** **a** Colour contour plots of the azimuthally-averaged magnetic diffraction ring intensity profiles, after form-factor normalization, as a function of both time and radial  $q$  for the first- and third-order rings. The first- and third-order rings are presented in the bottom and top panel, respectively. The dashed red line marks the average ring radius prior to optical pump. The dashed black line marks the ring radius averaged between 6 ps and 11 ps after optical pump. A shift in both rings is detected;  $0.0018 \pm 0.0001 \text{ nm}^{-1}$  for the first-order ring and  $0.0054 \pm 0.0003 \text{ nm}^{-1}$  for the third-order ring. **b** Data and fits in the representation of equation (2) shown by, respectively, solid black and dashed red curves. Time instances at 0 ps,

1.6 ps, and 18.8 ps are shown and shifted vertically for clarity. The positions of the first-, third-, and fifth-order diffraction rings at equilibrium are shown by vertical black dashed lines. The position of the first and third diffraction ring from the raw experimental data is pinpointed by black circles. Inferior fits by use of the domain-wall broadening model of [14] are shown by blue curves. The time evolution of the domain width  $w_d$  and diffraction-ring width  $\Gamma$  are shown in panels **c** and **d**. In both panels **c** and **d**, the vertical dashed black lines indicate  $t = 0$  and  $t = 10$  ps. Error bars represent one standard deviation.

**Figure 5. Domain dilation.** **a** Schematic of the proposed inelastic scattering process. In the reference frame of a quasi-ballistic electron, a Doppler shift causes the domain network to appear as a propagating magnon ensemble with a well-defined momentum. In the event of magnon-electron scattering, conservation of momentum requires that the reduction in electron momentum in the laboratory rest-frame leads to a commensurate coherent recoil of the Doppler-shifted magnon momentum. **b** Snapshots of the magnetisation profile obtained from the Bloch domain-wall model of equation (3) at various times. The dashed black curve is the equilibrium domain. Quenching, domain-wall broadening, and domain dilation after optical pumping are all evident by eye. **c** Maximum magnetisation obtained from the Bloch wall model of equation (3) (solid blue curve and circles), as compared with the experimentally-measured time-resolved XMCD (solid red curve and circles) from the same sample when subjected to an *in situ* saturating perpendicular magnetic field. The domain pattern in zero field quenches by 15% more than the saturated state at 1.6 ps. Error bars represent one standard deviation.

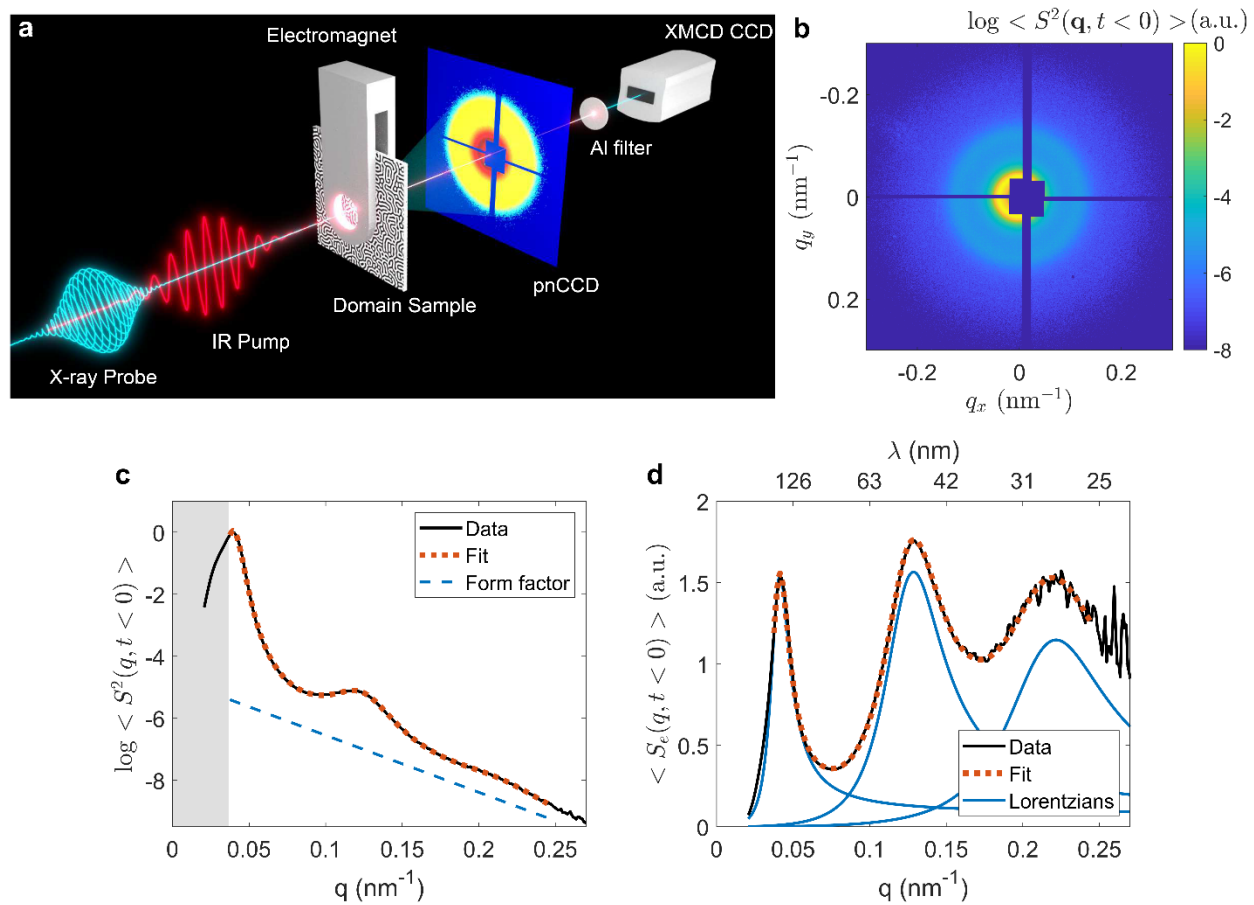


**Figure 1**



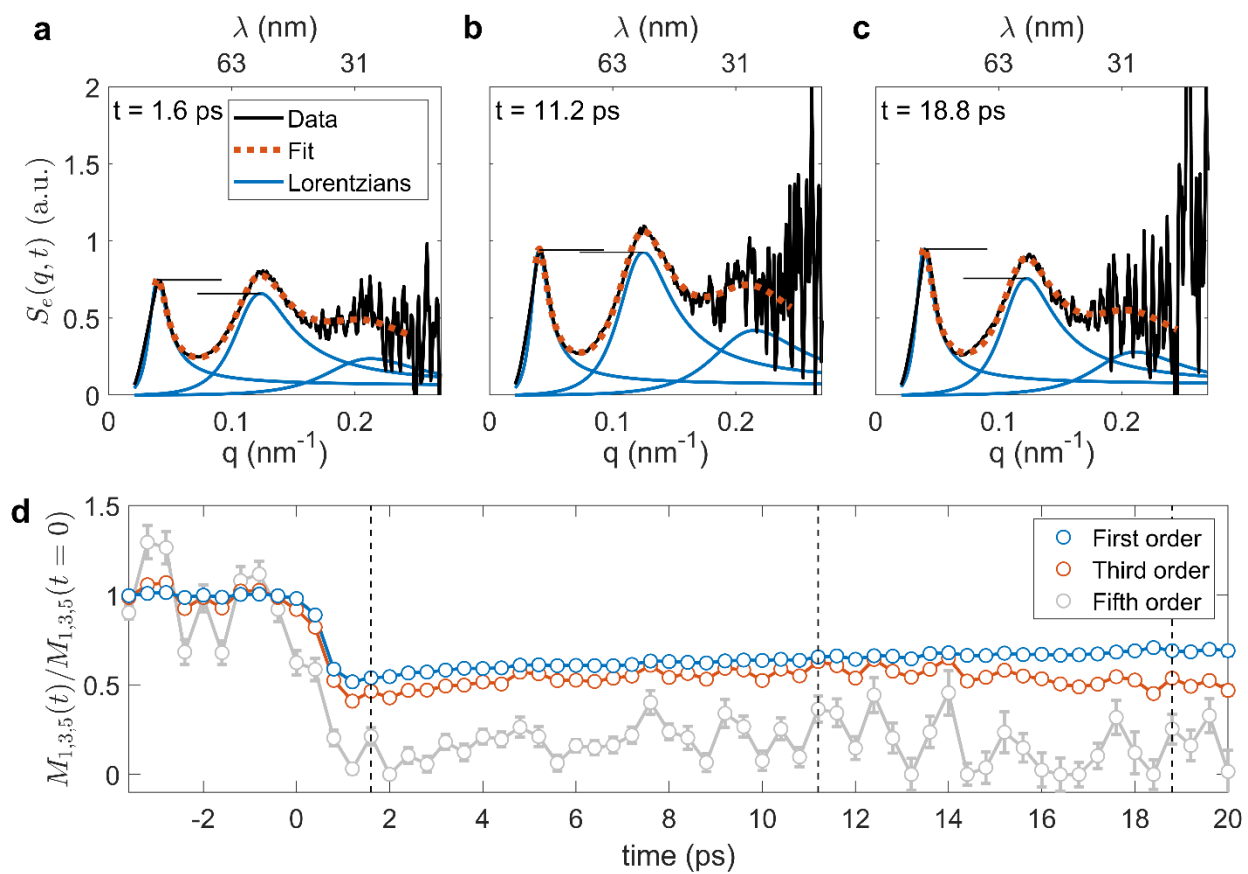


Figure 2.

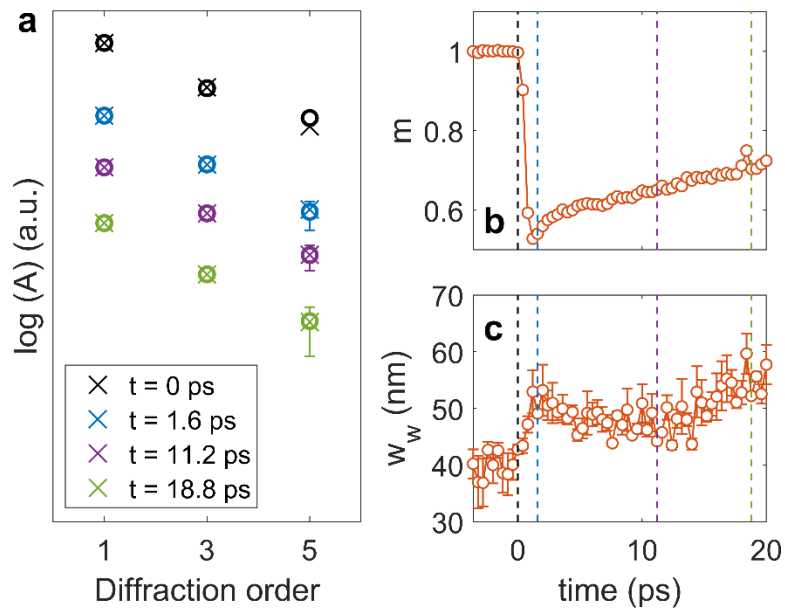
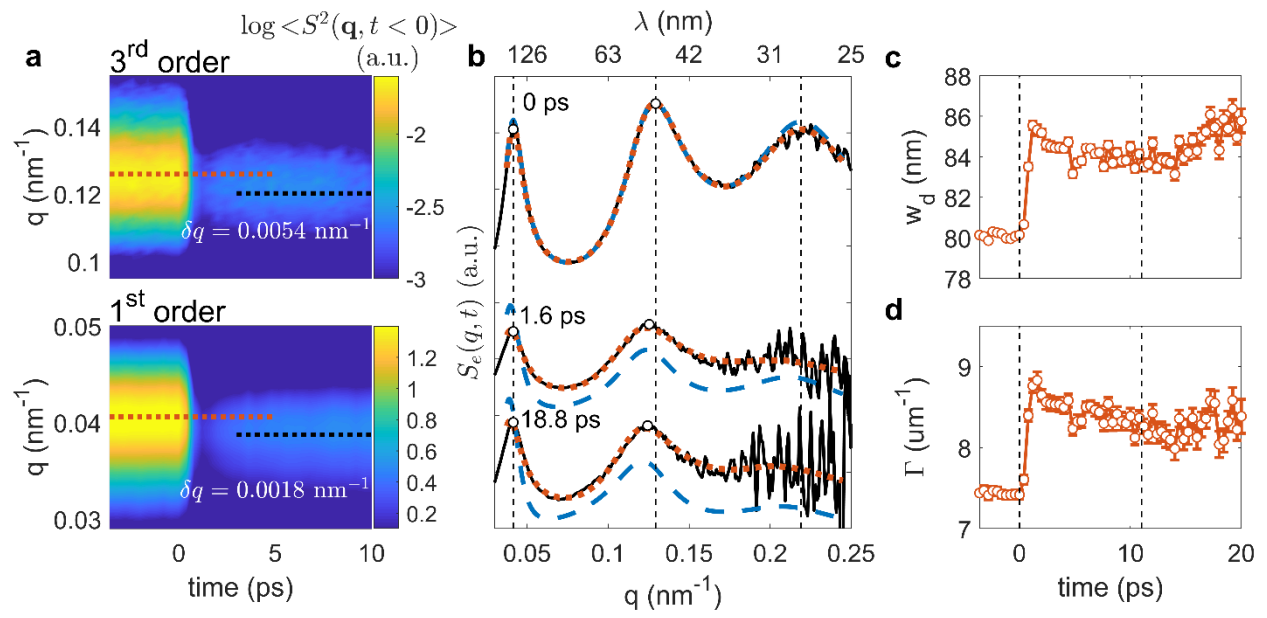


Figure 3.



**Figure 4**

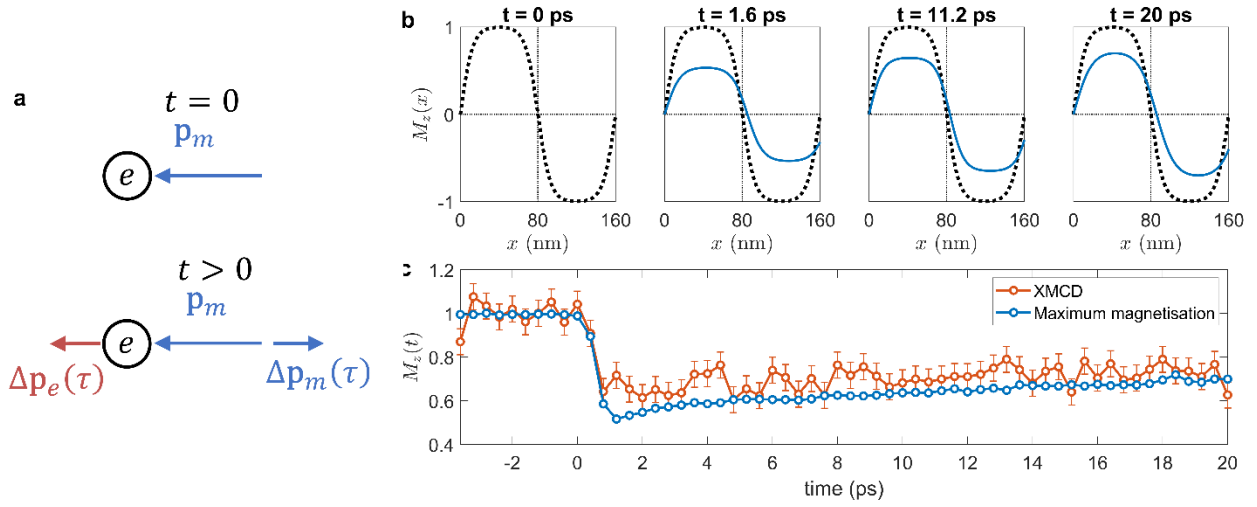


Figure 5

**Ultrafast domain dilation induced by optical pumping in ferromagnetic CoFe/Ni multilayers**

Zusin et al.

## Supplementary Note 1. Subtraction of charge contribution to the scattering intensity

To separate the electronic and magnetic contributions, we use the refractive index formalism to describe the interaction of soft X-rays with the ferromagnetic multilayer film. An equivalent description in terms of scattering amplitudes is also possible [1].

Within the approach adopted here, spatial variations of the refractive index  $n_0$  will cause the incident X-rays to scatter. The variations could either be caused by inhomogeneities of the chemical composition or surface roughness, collectively referred to as charge variations  $c(\mathbf{r})$ , where  $\mathbf{r} = (x, y)$  is the spatial coordinate, or a spatially dependent profile of the out-of-plane magnetisation component  $s(\mathbf{r}) \equiv M_z(\mathbf{r})$ .

With the corrections to the refractive index  $\delta n_c$  and  $\delta n_s$  due to charge and spin variations, respectively, the electric field of an electromagnetic wave transmitted through the sample is

$$E = E_0 \exp[ikd(n_0 + \delta n_s s(\mathbf{r}) + \delta n_c c(\mathbf{r}))], \quad (1)$$

where  $E_0$  is the incident circularly polarized wave and is assumed to be a plane wave ( $E_0 = 1$ ) due to the large spot size of the incident beam of  $\sim 100 \mu\text{m}$  relative to its wavelength of 1.45 nm,  $d$  is the sample thickness, and  $k$  is the wavenumber of the incident X-rays.  $E$  in equation (1) is referred to as the exit surface wave (ESW). We divide out the term  $\exp[ikd n_0]$  and, to make the notation more compact, introduce substitutions  $C(\mathbf{r}) = ikd\delta n_c c(\mathbf{r})$  and  $S(\mathbf{r}) = ikd\delta n_s s(\mathbf{r})$ . A Taylor expansion of equation (1) to first order in  $C(\mathbf{r})$  and  $S(\mathbf{r})$  yields

$$E = 1 + C(\mathbf{r}) + S(\mathbf{r}). \quad (2)$$

The scattered intensity at the detector is obtained by taking a Fourier transform of equation (2) and multiplying it by the conjugate

$$I_q = |C(\mathbf{q})|^2 + |S(\mathbf{q})|^2 + 2\text{Re}(C(\mathbf{q})S(\mathbf{q})), \quad (3)$$

where  $C(\mathbf{q})$  and  $S(\mathbf{q})$  are Fourier transforms of  $C(\mathbf{r})$  and  $S(\mathbf{r})$ , respectively. The Fourier transform of the first term in equation (2) is a delta function  $\delta(\mathbf{q})$ , which is non-zero only when the scattering vector  $\mathbf{q} = 0$ . Since we are not interested in the unscattered signal, we neglected the delta function in equation (3).

Because the incident X-ray probe is circularly polarized, the magnetically and electronically scattered X-rays have the same polarization, and thus the third term in equation (3) is, in general, non-zero.

When a saturating perpendicular magnetic field  $H_z$  is applied to the sample, it eliminates the magnetic domains, and the complex magnetically scattered signal  $S(\mathbf{q})$  vanishes except at  $\mathbf{q} = 0$ , in which case  $I(\mathbf{q}) \propto |C(\mathbf{q})|^2$ . However, the total transmission through the sample still depends on its magnetisation direction due to the effect of X-ray magnetic circular dichroism upon circularly polarized X-rays, which in turn affects the charge scattering because of the non-zero sample thickness. Thus, the magnitude of the scattered intensity is essentially a product of the charge scattering and a field-dependent XMCD transmission factor  $I_{\text{XMCD}}(H_z)|C(\mathbf{q})|^2$ . This variation can be accounted for by including second order terms in the Taylor expansion of equation (2), as was done in Ref. [5]. For that reason, the pure charge scattering  $|C(\mathbf{q})|^2$  with circular polarized X-rays and a non-negligible sample thickness is found from the scattering intensities taken with positive and negative applied saturating fields

$$\Sigma = \frac{1}{2} [I(\mathbf{q}, +H_z) + I(\mathbf{q}, -H_z)] = |C(\mathbf{q})|^2. \quad (4)$$

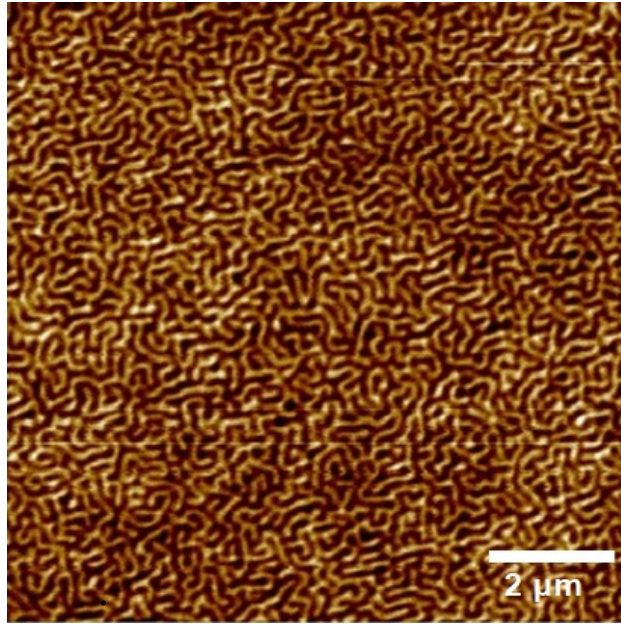
A relatively weak charge scattering ring was observed when the sample was saturated in an applied magnetic field, with a ring radius of  $q = 0.2 \text{ nm}^{-1}$ , corresponding to the grain size of the sputtered polycrystalline sample. The charge scattering overlap was confined to the relatively weak fifth-order magnetic-domain diffraction ring. For this reason, the effect of cross-terms in equation

(3) on the magnetic first- and third-order diffraction rings is negligibly small. We then extract the magnetic scattering intensity as

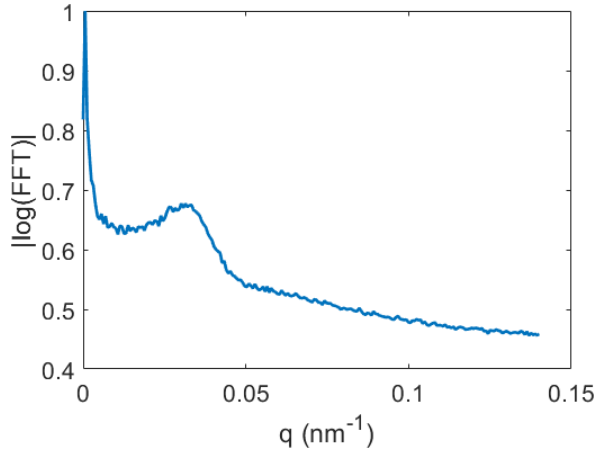
$$|S(\mathbf{q})|^2 = I(\mathbf{q}, H_z = 0) - \Sigma. \quad (5)$$

### Supplementary Note 2. Domain size from direct imaging

A direct image of a labyrinth domain pattern was obtained by means of magnetic force microscopy (MFM) with a similar sample, shown in the Supplementary Figure 1. In this measurement, the spatial resolution was approximately 22 nm. Upon contrast optimization of the MFM image and azimuthal average of its Fourier transform, we obtain the spatial spectral curve shown in the Supplementary Figure 2. This sample was deposited under similar conditions as the sample used for the X-ray scattering measurements. By visual inspection of the MFM spatial spectrum, we estimate a peak Fourier amplitude for the domain pattern, adjusted for the  $q$ -dependent background amplitude, at  $q_0 = 0.033 \text{ nm}^{-1} \pm 0.002 \text{ nm}^{-1}$ . This is equivalent to a domain size of  $95 \text{ nm} \pm 7 \text{ nm}$ , in fair agreement with the  $w_d \cong 80.14 \pm 0.04 \text{ nm}$  obtained for  $t < 0$  from X-ray scattering with a similar sample.



**Supplementary Figure 1.**  $10 \times 10 \mu\text{m}^2$  magnetic force microscope (MFM) image of a similar CoFe/Ni multilayer sample to that used for the X-ray scattering measurements.



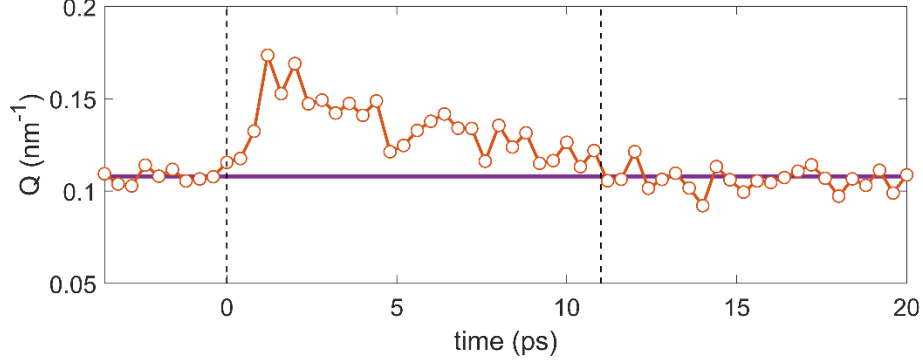
**Supplementary Figure 2. Azimuthally averaged Fourier transform of real-space MFM domain micrograph presented in Supplementary Figure 1.**

### **Supplementary Note 3. Time evolution of the form factor, $Q$**

The form factor at equilibrium is concurrently fitted with the Lorentzian line shapes and returns a value of  $Q(0) = 0.1087 \text{ nm}^{-1} \pm 4.48 \times 10^{-5} \text{ nm}^{-1}$ . The exponential form factor corresponds to a spatial distribution of spin density with a Lorentzian-like correlation function which may be interpreted as an approximation of the exchange length,  $\lambda_{ex} \approx 1/Q = 9.19 \text{ nm} \pm 0.0038 \text{ nm}$ , in rough agreement with the calculated exchange length of 7.3 nm determined from a combination of magnetometry measurements and an assumed exchange constant of  $A_{ex} = 2 \times 10^{-11} \text{ J m}^{-1}$ .

The time evolution of the form factor exponent  $Q$  is shown in the Supplementary Figure 3, exhibiting an ultrafast increase and subsequent recovery to equilibrium, shown by a solid magenta line, at  $\approx 10$  ps. It is possible this is the result of an ultrafast alteration in the characteristic exchange length of the sample, where the exchange length is defined as  $\lambda_{ex} \equiv \sqrt{2A_{ex}/\mu_0 M_s^2}$ , which is directly proportional to the exchange integral. If it is indeed the case that  $Q \propto 1/\lambda_{ex}$ , then it would suggest that the exchange stiffness is attenuated more than the magnetisation immediately after optical pumping. This is in agreement with previous studies that found significant evidence for a reduction in the exchange splitting in ultrafast pumping experiments [6,7]. The fact that  $Q$  returns to its equilibrium value 10 ps after pumping suggests that this is the time scale at which conventional equilibrium concepts relating temperature, magnetisation, and the renormalization of exchange, i.e.,  $A \propto M_s$ , are valid [8-10]. Coincidentally, 10 ps is the time scale at which the electron, spin, and lattice thermal baths are generally considered to be in thermal equilibrium with each other.





**Supplementary Figure 3. Time evolution of the fitted form factor.** The magenta solid line indicates the pre-pump equilibrium value for  $Q$ . The dashed vertical black lines indicate  $t = 0$  ps and  $t = 10$  ps, when  $Q$  recovers its pre-pump value.

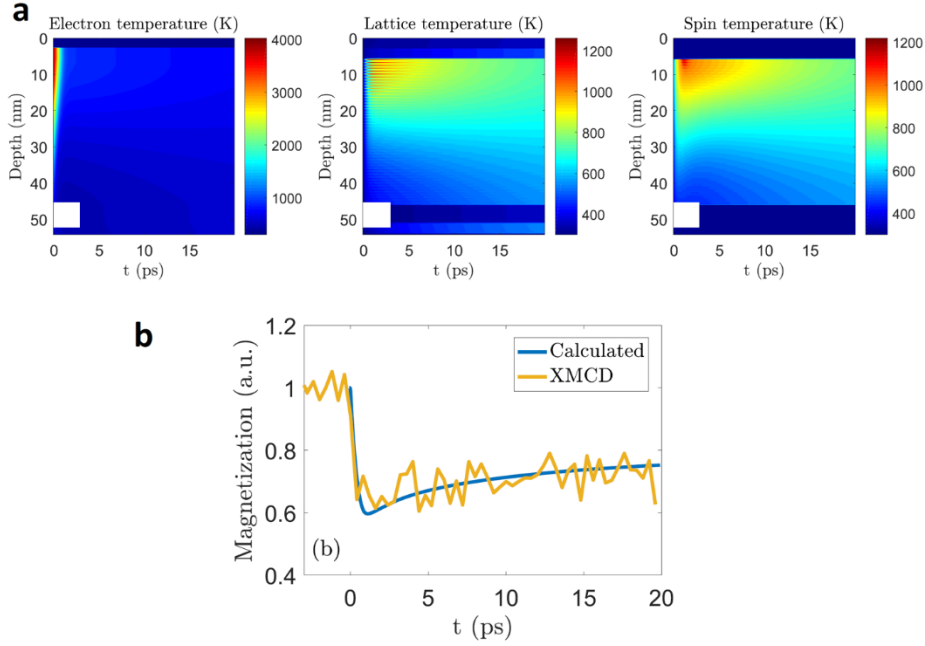
#### Supplementary Note 4. Time evolution of thermal profile in thick metallic multilayers after optical pumping

The heat transport in the film was modelled by use of the three-temperature model [11], which includes three coupled equations to describe the dynamics of the electron, lattice, and spin temperature baths

$$\begin{aligned}
 C_e(T_e) \frac{\partial T_e}{\partial t} &= \vec{\nabla} \cdot (\kappa_e(T_e, T_l) \vec{\nabla} T_e) + G_{el}(T_e)(T_l - T_e) + G_{es}(T_s - T_e) + S(z, t), \\
 C_l(T_l) \frac{\partial T_l}{\partial t} &= \vec{\nabla} \cdot (\kappa_l(T_e, T_l) \vec{\nabla} T_l) + G_{el}(T_e)(T_e - T_l) + G_{ls}(T_s - T_l), \\
 C_s(T_s) \frac{\partial T_s}{\partial t} &= G_{es}(T_e - T_s) + G_{ls}(T_l - T_s).
 \end{aligned} \tag{6}$$

We used material-specific and temperature-dependent values for the specific heat  $C_x$ , thermal conductivity  $\kappa_x$ , the electron-lattice coupling constant  $G_{el}$ , the electron-spin coupling constant  $G_{es}$ , and the lattice-spin coupling constant  $G_{ls}$  [5,12-14]. The subscript  $x$  stands for  $e$ ,  $l$ , or  $s$  to denote the electron, lattice, or spin system, respectively. The laminate structure of the sample was taken into account, and the spatial profile of the heat source  $S(z, t)$  was found by computing the absorption of the pump light with an incident fluence of  $26.7 \text{ J cm}^{-2}$  by the film using the multilayer formalism of Ref. [15]. More details on the material parameters used in the simulation can be found in Ref. [5]. The magnetisation profile was obtained from the calculated temperature of the spin system using the experimentally measured temperature dependence of the magnetisation. The electron-spin coupling parameter was chosen to be  $G_{es} = 3 \times 10^{17} \text{ W m}^{-3} \text{ K}^{-1}$  to obtain a good fit to the experimental XMCD signal, as shown in Supplementary Figure 4. However, one must take the calculated temperatures for the various thermal baths in this model to be no more than rough estimates at the short times over which substantial changes in the magnetic scattering occurs. Given that  $G_{es} \gg G_{ls}$ , and an estimated  $C_s(T_s) \cong 1.5 \times 10^6 \text{ J m}^{-3} \text{ K}^{-1}$  at the elevated temperatures expected after pumping, the estimated time constant for heat transfer between the electronic and spin system is 5 ps, which is much longer than the measured domain dilation time and the domain-wall broadening time of 1.6 ps. This highlights the fact that the electron-spin scattering processes

in the far-from-equilibrium regime are strongly amplified for this system when compared to those expected from highly simplified models based on equilibrium dynamics.



**Supplementary Figure 4. Thermal model results.** **a** Depth profile temperature results of three-temperature heat transport model for the electronic, lattice, and spin temperatures. **b** The electron-spin coupling coefficient was chosen to optimize the fit of the XMCD data for magnetisation vs. time, averaged over the depth of the sample.

### Supplementary Note 5. Time-dependent filtering kernels

In our measurements, we were able to detect all three orders of diffraction rings at all times after the femtosecond optical pulse. This fact allows us to test the hypothesis brought forth by Pfau, *et al.*, [16] that their time-resolved distortions of the first-order diffraction ring could be plausibly explained in terms of a Gaussian filter function that attenuated high- $q$  components of the diffraction after pumping. Such a process would entail a domain-size-dependent demagnetisation. Because the Gaussian function applies to the domains, convolution with the domain-wall profile leads to the following functional form

$$f_G(q, t) = e^{-2q/\langle Q(t<0) \rangle} \left[ \langle M_0(t < 0) \rangle + \sum_{n=0}^2 \frac{M'_{2n+1}(t)}{\left( \frac{q - (2n+1)\langle q_0(t<0) \rangle}{(2n+1)\langle \Gamma(t<0) \rangle} \right)^2 + 1} e^{-2q^2/2((2n+1)\sigma(t))^2} \right]^2 \quad (7)$$

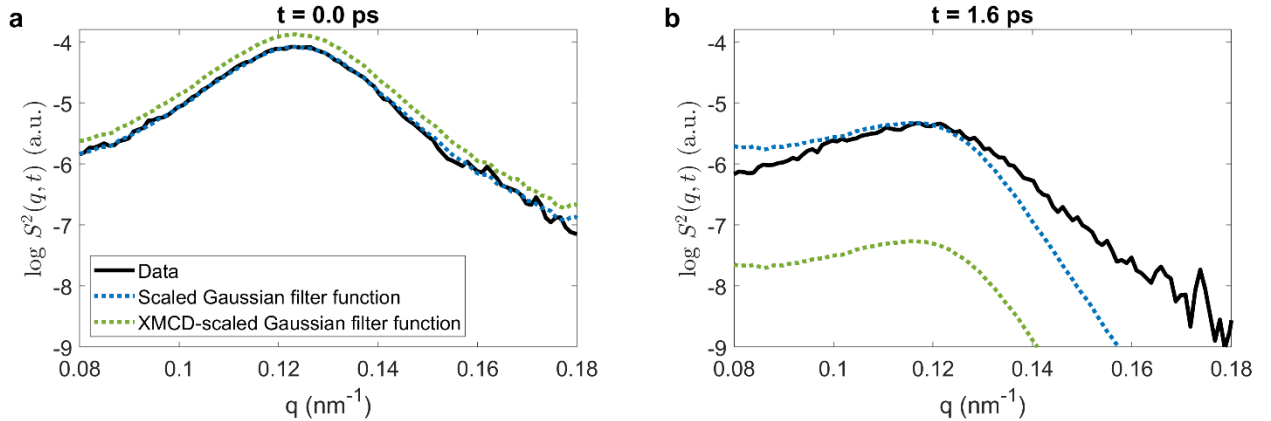
where the quantities  $M_{2n+1}(t)$  are fitting parameters and  $\sigma(t)$  is the Gaussian standard deviation. Note that only the Gaussian filter function is time dependent while the remaining parameters can be estimated from the fit to  $\langle S^2(q, t < 0) \rangle$ . As shown in the text, this functional form does not faithfully represent the data.

Use of a Gaussian function is advantageous because it is possible to analytically solve for  $\sigma(t)$  to produce the observed peak shift. With this method, we can study more closely the implications of invoking a Gaussian filter function. In particular, we are interested to test whether

this representation is valid for the third-order ring, which was not measured in Ref. [16]. For this, we use the analytical form of the Gaussian standard deviation

$$\sigma(t) = (\Gamma(t)^2 + |q_0(t) - \langle q_0(t < 0) \rangle|^2) \left( \frac{q_0(t)}{|q_0(t) - \langle q_0(t < 0) \rangle|} - 1 \right) \quad (8)$$

as a function of the fitted linewidth  $\Gamma(t)$  and ring radius  $q_0(t)$ . We then isolate the third order ring from the data by subtracting the first and fifth-order rings as well as the form factor and background fitted with  $f(q,t)$ , equation (1) in the main text. This data is shown in the Supplementary Figure 5 by solid black curves. At  $t = 0$ , shown in panel **a**, the data is slightly asymmetric because of the residue from the first-order ring fit. Note that this is not the time-averaged data for  $t < 0$ , but the data captured at  $t = 0$  with respect to the pump pulse. The spectrum obtained by using a Gaussian filter function is shown by dashed blue curves. For this, we use the pre-pump ( $t < 0$ ) *time-averaged* data for the third-order ring, multiply it by a Gaussian filter function with standard deviation given in equation (8), and scale it so as to match the ring amplitude at  $q_0(t)$ . Good agreement is obtained at  $t = 0$ , shown in panel **a**. This is expected since in the absence of a shift, the equation (8) tends to infinity. However, for  $t = 1.6$  ps shown in panel **b**, we clearly see an asymmetry. This asymmetry appears because a Gaussian filter function physically implies that small domains demagnetise more than large domains. This asymmetry also renders  $f_G(q,t)$  unable to accurately fit the experimental data, as shown in the main text, Figure 4. An even poorer agreement is obtained by scaling the Gaussian filter function by the measured XMCD data, shown by green dashed curves. The rationale of this approach is that the filter function at  $\mathbf{q} = 0$  should be proportional to the quenching for a uniformly magnetized sample to be a complete description of the ultrafast demagnetization.



**Supplementary Figure 5. Third-order ring spectra obtained by use of Gaussian filter function.** In both panels, the black curves are data, blue dashed curves are spectra obtained with a suitably scaled Gaussian filter function, and the green dashed curves are spectra obtained by Gaussian filter functions scaled by the experimental XMCD data.

Another approach to a filter function is to reconstruct it from experimental data. The hypothesis in Ref. [16] was based on linear response theory, where the dynamic evolution of the domain network is attributed to a time-dependent spatial filter kernel  $G(x, y, t)$  that is convolved with the equilibrium perpendicular-to-plane magnetisation component

$$M_z(x, y, t) = G(x, y, t) * M_z(x, y, t = 0) \quad (9)$$

Because the scattering intensity is related to  $M_z$  via a Fourier transform,  $|S(\mathbf{q}, t)|^2 = |\mathcal{F}\{M_z\}|^2$ , it is possible to reinterpret the filtering kernel as a multiplicative factor in Fourier space  $g(\mathbf{q}, t)$  that describes the time-dependent evolution of the scattering, given by

$$g(\mathbf{q}, t) = \sqrt{|S(\mathbf{q}, t)|^2 / |S(\mathbf{q}, t = 0)|^2} \quad (10)$$

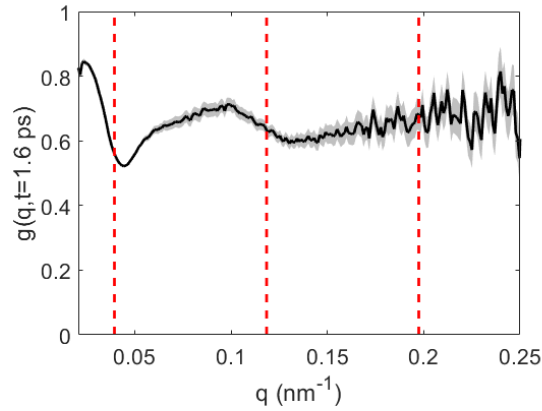
where  $g(\mathbf{q}, t) = \mathcal{F}\{G(x, y, t)\}$ . This kernel may be computed from experimental data with good accuracy up to the third-order peak. However, employment of the filter in equation (10) with our diffraction data yields a complicated transfer function with multiple maxima and minima that deviates significantly from a Gaussian functional form. An example filtering kernel obtained at 1.6 ps after the pump pulse is shown by a solid black curve in the Supplementary Figure 6.

The associated error to the kernel can be computed by standard error propagation to be

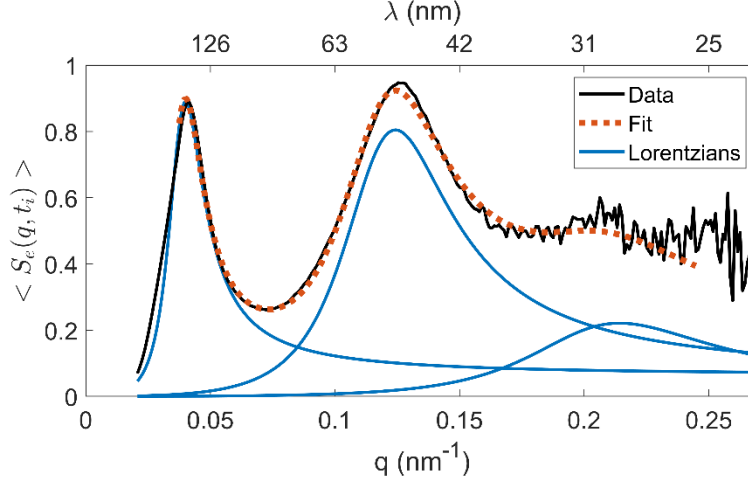
$$\delta g(\mathbf{q}, t) = \frac{1}{\sqrt{N(\mathbf{q})}} \frac{g(\mathbf{q}, t)}{2} \sqrt{\frac{1}{g(\mathbf{q}, t)^2} + 1} \quad (11)$$

where  $N(\mathbf{q})$  is the time-independent photon count per  $q$  and we assume that the main source of noise in the measurement is shot noise. The error is shown in grey colour in the Supplementary Figure 6. While the low- $q$  portion of the filtering kernel for  $q < 0.04 \text{ nm}^{-1}$  appears Gaussian, the qualitative behaviour is distinctly non-Gaussian for higher  $q > 0.04 \text{ nm}^{-1}$ .

While the filter function  $g(\mathbf{q}, t)$  may allow to find a functional form that fits the data, its most salient shortcoming is lack of generality: the filter function cannot explain both our measurements and the measurements obtained in Ref. [16]. We therefore conclude that extraction of the filter function  $g(\mathbf{q}, t)$  is not a viable method for the determination of how optical pumping affects demagnetisation in the presence of a labyrinth domain pattern.



**Supplementary Figure 6. Time-dependent filtering kernel computed from experimental data at  $t = 1.6 \text{ ps}$ .** Vertical dashed red lines indicate the positions of the first-, second-, and third-order diffraction rings at  $t < 0 \text{ ps}$ .



**Supplementary Figure 7. Fits of time averaged scattering data after pumping.** The equalized, azimuthal-average data are time-averaged in the interval  $t_i = [6 \text{ ps}, 11 \text{ ps}]$ . The equalized data, fits, and Lorentzians in the representation of equation (2) in the main text are shown by solid black, dashed red, and solid blue curves, respectively. After time-averaging, the fifth-order ring, though significantly quenched relative to what is detected prior to pumping (e.g. the upper panel in Figure 4b in the main text), is more clearly distinguished, and is found to be resolved in a manner that is consistent with the fitting of the first- and third-order rings. Small errors in the fit with increasing  $q$  are visibly enhanced in this equalized representation. Regardless, the fit is extremely sensitive to the exact positions of the diffraction rings in the data, as captured with the Lorentzian model for the ring profiles. In this particular fit, we obtained  $q_0 = 0.0373 \text{ nm}^{-1} \pm 4.5 \times 10^{-5} \text{ nm}^{-1}$ , corresponding to a domain width of  $84.1 \text{ nm} \pm 0.03 \text{ nm}$ . This represents a  $\cong 4\%$  domain dilation, in good agreement with the domain width of  $83.9 \text{ nm} \pm 0.3 \text{ nm}$  calculated from time-average of the domain width shown in Figure 4c in the main text within the time interval  $t_i$ .

### Supplementary Note 6. Hot electron momentum from ultrafast pumping

The momentum of hot electrons excited by ultrafast pumping is calculated from Ref. [17]. Within the first 500 ps, we expect electrons to remain quasi-ballistic insofar as electron-phonon scattering occurs on a time scale of 2-3 ps. The electron velocity in Ref. [17] is given by

$$\mathbf{v} = \frac{\mu k_B \vec{\nabla} T}{e} \quad (12)$$

Because the effective thermal electric field is  $\mathbf{E}_{\text{eff}} = \frac{k_B}{e} \vec{\nabla} T$ , then we can write the momentum as

$$\langle \mathbf{p}_e(t) \rangle = \mathbf{F}t = e\mathbf{E}_{\text{eff}}t = k_B \vec{\nabla} T t \quad (13)$$

For an effective temperature gradient of 3000 K over 170  $\mu\text{m}$  in 1 ps, the average radial electron momentum  $\langle \mathbf{p}_e(t) \rangle / \hbar$  is  $2.3 \mu\text{m}^{-1}$ , or 6% of  $q_0 = 39.2 \mu\text{m}^{-1}$ .

## Supplementary Note 7. Energy conservation

Both momentum- and energy-conservation must be considered for an inelastic scattering process. Here, we provide a highly simplified estimation of the possible deformation of the domain structure that can be driven by the available kinetic energy of the radially flowing ballistic-like hot-electron flow.

The far-from-equilibrium net kinetic energy of the ballistic-like hot electrons excited by the pump pulse is given by

$$E_e = \frac{1}{2} m_e v_e^2 = \frac{1}{2m_e} \left( \frac{k_B T_e \tau}{w} \right)^2 \quad (14)$$

where  $\tau$  is the momentum scattering time. The kinetic energy density associated with this net radial electron flow is

$$U_e = n_e E_e \quad (15)$$

Using a conduction electron density of  $n_e \approx 9 \times 10^{28} \text{ m}^{-3}$ , we arrive at an available energy density of  $U_e = 2.9 \text{ kJ m}^{-3}$ .

The energy of a Bloch wall is given by

$$U_{\text{Bloch}} = \pi \sqrt{A_{\text{ex}} K_u} \quad (16)$$

where  $A_{\text{ex}}$  is the exchange energy density.  $U_{\text{Bloch}}$  is an energy per unit area of the domain wall. For a wall of length  $L$  in a film of thickness  $d$ ,  $U_{\text{Bloch}}$  is multiplied by the product  $Ld$  to obtain the net energy of the wall. The width of a Bloch wall is given by

$$w_w = \pi \sqrt{A_{\text{ex}} / K_u} \quad (17)$$

We approximate the equilibrium energy density of the labyrinth domain structure  $U_d$  as a close-packed network of Bloch walls that are spaced  $w_w$  apart, centre to centre. From this, the spatially averaged domain wall energy density is

$$U_d \approx \frac{U_{\text{Bloch}}}{w_w} = K_u \quad (18)$$

Using a Taylor series expansion of the energy about equilibrium in two dimensions, we end up with a non-equilibrium energy density  $\Delta U_w$  associated with the domain dilation  $\Delta w_d$  of

$$\Delta U_d \cong 2K_u \left( \frac{\Delta w_d}{w_d} \right)^2 \quad (19)$$

The factor of two comes from the fact that a change in the linear density of the domain wall density causes a change in the two-dimensional energy density. For the measured domain expansion of 6%, we have  $\Delta U_d = 0.7 \text{ kJ m}^{-3}$ , in which case the kinetic energy of the electrons is more than sufficient to drive the observed domain dilation. The excess electron energy can drive further widening of the domain walls that is not compensated by domain dilation, which could further explain the observed broadening of the domain-walls.

Appealing again to the Taylor series expansion approach, the non-equilibrium energy density  $\Delta U_w$  associated with domain-wall broadening *without a compensating change in domain density* is

$$\Delta U_w \cong K_u \left( \frac{\Delta w_w}{w_w} \right)^2 \quad (20)$$

If we assume that all the excess electron energy drives domain-wall broadening, then the resultant broadening would be

$$\left( \frac{\Delta w_w}{w_w} \right) = \sqrt{\frac{U_e - 2K_u \left( \frac{\Delta w_d}{w_d} \right)^2}{K_u}} \cong 15\% \quad (21)$$

By fitting of our data to the hyperbolic tangent model, we measured a broadening of 31% within 1.6 ps. Thus, half of the observed ultrafast broadening of the domain walls can be attributed to the residual electronic kinetic energy after momentum transfer to the domain structure is taken into account.

## References:

- [1] Tesch, M. F. et al. X-ray magneto-optical polarization spectroscopy: an analysis from the visible region to the X-ray regime. *Appl. Optics* **52**, 4294 – 4310 (2013)
- [2] Granitzka, P. W. et al. Magnetic switching in granular FePt layers promoted by near-field laser enhancement. *Nano Letters* **17**, 2426 – 2432 (2017)
- [3] Reid, A. H. et al. Beyond a phenomenological description of magnetostriction. *Nature Commun.* **9**, 388 (2018)
- [4] Liu, T.-M. et al. Nanoscale confinement of all-optical magnetic switching in TbFeCo. *Nano Letters* **15**, 6862 – 6868 (2015)
- [5] Zusin, D. Ultrafast dynamics of Magnetic multilayer films: magneto-optical spectroscopy and resonant scattering in the extreme ultraviolet and soft X-ray spectral regions. (University of Colorado Boulder, 2018)
- [6] Turgut, E. et al. Controlling the competition between optically induced ultrafast spin-flip scattering and spin transport in magnetic multilayers, *Phys. Rev. Lett.* **110**, 197201 (2013)
- [7] Turgut, E. et al. Stoner versus Heisenberg: ultrafast exchange reduction and magnon generation during laser-induced demagnetization. *Phys. Rev. B* **94**, 220408 (2016)
- [8] Bloch, M. Magnon Renormalization in Ferromagnets Near the Curie Point. *Phys. Rev. Lett.* **9**, 286--287 (1962)
- [9] Lowde, R. D. Spin Waves and Neutron Scattering. *Journal of Applied Physics* **36**, 884-892 (1965)
- [10] Stringfellow, M. W. Observation of spin-wave renormalization effects in iron and nickel. *Journal of Physics C: Solid State Physics* **1**, 950 (1968)
- [11] Beaurepaire E., Merle, J.-C., Daunois, A., & Bigot, J.-Y. Ultrafast Spin Dynamics in Ferromagnetic Nickel. *Physical Review Letters* **76**, 4250–4253 (1996)
- [12] Anisimov, S. I. & Rethfeld, B. Theory of ultrashort laser pulse interaction with a metal. *International Society for Optics and Photonics* **3093**, 192 – 204 (1997)

- [13] Ivanov, D. S. & Zhigilei, L. V. Combined atomistic-continuum modeling of short-pulse laser melting and disintegration of metal films. *Physical Review B* **68**, 064114 (2003)
- [14] Lin, Z., Zhigilei, L. V., & Celli, V. Electron-phonon coupling and electron heat capacity of metals under conditions of strong electron-phonon nonequilibrium. *Physical Review B* **77**, 075133 (2008)
- [15] Zak, J., Moog, E. R., Liu, C., & Bader, S. D. Magneto-optics of multilayers with arbitrary magnetization directions. *Physical Review B* **43**, 6423 (1991)
- [16] Pfau, B. et al. Ultrafast optical demagnetisation manipulates nanoscale spin structure in domain-walls. *Nat. Commun.* **3**, 110 (2012)
- [17] Najafi, E., et al. Super-diffusion of excited carriers in semiconductors. *Nature Communications* **8**, 15177 (2017)